A Bidirectional LLCL Resonant DC-DC Converter With Reduced Resonant Tank Currents and Reduced Voltage Stress of the Resonant Capacitor

XIAOCHEN MA[ID], **PING WANG**[ID], **(Member, IEEE), HUAKUN BI**[ID], **(Member, IEEE), AND ZHISHUANG WANG**

School of Electrical and Information Engineering, Tianjin University, Tianjin 300072, China

Corresponding author: Ping Wang (pingw@tju.edu.cn)

ABSTRACT In this paper, a bidirectional inductor-inductor-capacitor-inductor (LLCL) resonant dc-dc converter is presented. Compared with the conventional LLC, a parallel-connected inductors structure is employed into the resonant tank. By virtue of this unique resonant tank, LLCL exhibits the following desirable features: 1) good voltage gain regulation capability in bidirectional power flow applications; 2) zero-voltage-switching turn-on of the power switches in a wide load range; 3) compared with the other bidirectional LLC-type resonant converters, lower resonant tank currents and lower resonant capacitor voltage stress are achieved under the same working conditions. The topology derivation and operating principles of LLCL are shown, and the vital characteristics of LLCL are especially discussed. Moreover, based on battery applications in energy storage systems, in order to make the voltage gain range of LLCL meet the requirements while minimizing the resonant tank currents, a parameter design method is conducted. Finally, a 500-W prototype is established to verify the operating principles and design effects of the proposed converter.

I. INTRODUCTION

For promotion of the energy revolution, development of the energy storage systems (ESSs) has become one of the mainstream solutions [1]–[3]. In these systems, bidirectional dc-dc converters (BDCs) usually play an important role. Faced with diverse voltage levels and variation ranges, BDCs can ensure the reliable connection between the dc bus and the energy storage devices such as batteries. In addition, BDCs can also transmit bidirectional power between the dc bus and the batteries [4]. Energy utilization rate is therefore improved by the implementation of peak-clipping and valley-filling. Thus, the research on BDCs will become one of the most promising directions for developing ESSs [5]–[7].

Depending on whether a high-frequency transformer (HFT) is utilized for galvanic isolation, BDCs can be classified into

The associate editor coordinating the review of this manuscript and approving it for publication was Liu Hongchen[ID].

non-isolated BDCs and isolated BDCs. Since the voltage mismatch between the dc bus and the batteries in ESSs is great, HFT is often required for system safety and voltage-matching [8]. Thus, only isolated BDCs (IBDCs) are discussed in this paper. In a variety of IBDCs, the dual active bridge (DAB) converter is a basic type. DAB can realize bidirectional power flow and voltage gain regulations under the phase shift control [9], [10]. However, this control strategy will lead to a high reactive power, a limited zero-voltage-switching (ZVS) range and great turn-off losses, which will reduce the conversion efficiency. As a result, various improvements have been proposed. To minimize the reactive power, the global optimal phase shift ratios under four scenarios (forward/backward, buck/boost) are proposed in [11]. To broaden the ZVS range, the auxiliary LC networks and the auxiliary coupling inductor are employed into DAB in [12] and [13], respectively. However, although the ZVS range has been broadened, the complexity of the control strategies and

topology structures has increased significantly. Meanwhile, all the above solutions cannot effectively reduce the turn-off losses. Considering that the sinusoidal current waveform can obviously reduce the turn-off current, resonant converters have become a promising candidate for soft-switching applications. To minimize the phase difference between bridge currents and voltages, thereby reducing the reactive power, LCL and CLC resonant networks are employed into DAB in [14] and [15], respectively. Based on series resonant converter [16], [17], a phase shift and modified pulse-width modulation strategy has been proposed in [16], which simultaneously reduce the resonant tank current and extend the ZVS range. In [17], zero reactive power, minimum tank current, and complete soft-switching are all achieved by modulating the internal, external phase shift and switching frequency. However, since none of the topologies above can simultaneously obtain a wide soft-switching range, a simple control strategy and a good voltage regulation capability, compromises are often needed. Fortunately, these requirements can be fully achieved on LLC-type resonant converters. The conventional LLC can realize a wide ZVS range and a good voltage gain regulation under the simple pulse frequency modulation (PFM) method [18]. In addition, CLL converter can be also regarded as an LLC-type converter due to the similar conditions, such as the series-parallel resonant structure, gain, and soft-switching features [19], [20]. Unfortunately, since the voltage gain in forward mode and backward mode are not consistent, the conventional LLC-type converters are limited in bidirectional applications. To solve this problem, it is a great idea to improve the resonant tank and finally obtain a bidirectional LLC-type structure. Based on this idea, by adding extra capacitors or inductors, two typical state of the art LLC-type IBDC topologies have gained much attention:

A. BIDIRECTIONAL LLC (BI-LLC) RESONANT TOPOLOGY [21]–[24]

By adding an extra inductor in parallel with the input port of the conventional LLC resonant tank, Bi-LLC topology is firstly presented in [21] by Jiang *et al*. Since the topology is equivalent to a parallel structure of an LLC resonant tank and an inductor in both directions, the excellent features of LLC can be extended to bidirectional power flow applications. To further improve the voltage gain regulation capability, a fixed-frequency pulse-width modulation control method is applied to Bi-LLC in [22]. Moreover, by combining Bi-LLC with boost/buck converter [23] or three-port converter [24], Bi-LLC has been fully utilized in more practical applications.

B. CLLC RESONANT TOPOLOGY [25]–[29]

Compared with LLC, this topology is proposed in [25] by arranging an extra pair of capacitor and inductor in series on the secondary side of the HFT. Since LLC structure in both directions can be obtained, CLLC has been widely used in charging systems [26]–[28]. By using a superimposed output structure and integrating CLLC with a buck/boost

circuit [29], the converter's voltage gain and dynamic performances are further enhanced.

Based on these two typical topologies, although the IBDCs' ZVS range, bidirectional voltage gain and power flow regulation capabilities have been improved, optimization on the resonant tank currents and the resonant capacitor voltage stress has not been considered yet. The excessive resonant tank currents will increase the power losses, and the high resonant capacitor voltage stress will not only increase the cost but also reduce the converter's reliability. Therefore, it is necessary to optimize the above two indicators. Based on this consideration, a novel bidirectional LLC-type resonant dc-dc converter, LLCL converter, is proposed in this paper. The proposed converter also has a simple structure and a simple control strategy. The remaining parts of this paper are organized as follows: Section II presents the LLCL topology derivation process and its operating principles. The characteristics analyses are shown in Section III. The parameter design ideas are explained in Section IV. In Section V, the experiment results based on a 500-W prototype are displayed. Finally, the conclusions are summarized in Section VI.

II. TOPOLOGY DERIVATION AND OPERATING PRINCIPLES

A. TOPOLOGY DERIVATION

According to the statement in Section I, for conventional LLC-type resonant converters, the resonant tanks of LLC and CLL can be shown in Fig. 1(a) and (b), respectively. For LLC-type IBDC converters, the resonant tanks of Bi-LLC and CLLC can be shown in Fig. 2(a) and (b), respectively. With regard to CLLC illustrated in Fig. 2(b), it can be noticed that in order to effectively utilize the magnetizing inductor of the transformer T to reduce the size of the total magnetic components, T should only be paralleled with L_a. Hence, one of the two resonant capacitors C_r and C_r' will inevitably be placed on the high voltage side, which may result in high capacitor voltage stress. Meanwhile, 5 resonant elements also make the structure complicated and cost increase. As a
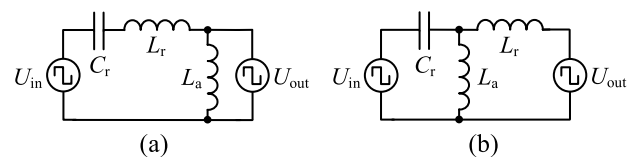

FIGURE 1. Conventional LLC-type resonant tanks. (a) LLC, (b) CLL.
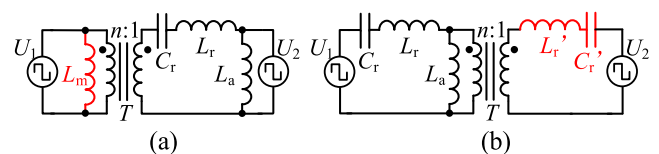

FIGURE 2. Two typical state of the art LLC-type IBDC resonant tanks. (a) Bi-LLC, (b) CLLC.

consequence, Bi-LLC has more advantages from these points of view. Thus, Bi-LLC rather than CLLC will be used as a breakthrough point for the derivation of the new topology.

For Bi-LLC shown in Fig. 2(a), the topology can be seen as adding an extra inductor L_m into the LLC resonant tank. Consequently, the LLC structure can be formed in both directions. However, since L_m and L_a are voltage-clamped by U_1 and U_2, respectively, L_m and L_a cannot affect the equivalent resonant inductance L_{eq} (because the voltages of L_m and L_a are square waveforms instead of sinusoidal waveforms). Therefore, for Bi-LLC, L_{eq} is equal to L_r.

To reduce the resonant tank currents, it can be achieved by increasing the resonant tank impedance. When the current through the resonant capacitor is reduced, the capacitor voltage stress will also decrease under the same capacitance value. From this perspective, it thus seems to be a good solution by increasing the inductance values of the resonant tank. However, for Bi-LLC, if the inductance of L_r is increased, the resulting increase in L_{eq} will change the resonant frequency, characteristic impedance, and quality factor, which in turn changes the working conditions of the converter. If the inductance of L_m or L_a is increased, according to [21], the converter's gain will change accordingly, which will also change the converter's working conditions. Hence, simply increasing the actual inductance values to increase the resonant tank impedance is not feasible. In other words, it is worthwhile to find a topology that has a bidirectional LLC-type structure while having a higher resonant tank impedance under the same working conditions.

For the purpose of increasing the resonant tank impedance, this paper proposes a basic idea. That is, based on Bi-LLC, if the connection way of L_m can be changed so that L_m is no longer voltage-clamped, L_m will affect L_{eq}. Further, from the perspective of the resonant currents flow paths, if L_m can form a parallel resonant relation with L_r, L_{eq} will decrease and be equal to L_m // L_r. Thus, in order to maintain the same L_{eq} (same working conditions) as Bi-LLC, the actual resonant inductance values of the new resonant tank need to be increased. Hence, compared with Bi-LLC, the new resonant tank will possibly have a higher impedance under the same working conditions.

Based on this idea, two derived topologies can be obtained and illustrated in Fig. 3. L_{eq} can be analyzed by the resonant currents. As can be seen from Fig. 3(a) and (b), the resonant currents can be divided into two main flow paths. For topology-1 shown in Fig. 3(a), starting from C_r, the first current path flows through L_m and U_1, and the second current path flows through L_r, L_a (or U_2), and U_1. For topology-2 in Fig. 3(b), starting from C_r, the first current path flows through L_a (or U_2) and L_m, and the second current path flows through L_a (or U_2), U_1, and L_r. Since L_a is voltage-clamped by U_2, L_a cannot affect L_{eq}. Thus, according to the resonant currents flow paths, it can be found that L_{eq} of the two derived topologies are both equal to L_m // L_r.

To ensure that the bidirectional LLC-type structure can be obtained, when power is transmitted from U_1 to U_2, it can
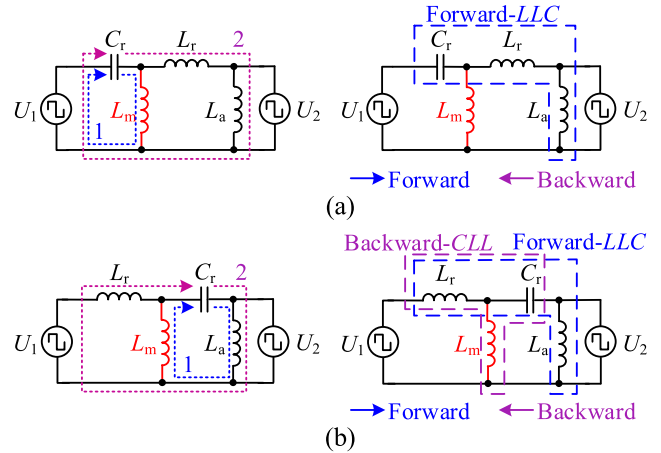

FIGURE 3. Newly derived resonant tank topologies. (a) Topology-1, (b) Topology-2.

be observed from Fig. 3(a) and (b) that both topologies can form an LLC structure by L_r, L_a, and C_r. However, when the power direction is reversed, only topology-2 can obtain a CLL structure by C_r, L_r, and L_m. To this end, the derived topology-2 shown in Fig. 3(b) is finally selected.

For the design of the overall topology, the following considerations are carried out:

a) To utilize the magnetizing inductor of the transformer T effectively, T should be paralleled with L_m or L_a.

b) To reduce the resonant capacitor voltage stress, C_r is arranged to the low voltage side (LVS).

c) To reduce the currents through the resonant inductors, it is necessary to place as many inductors as possible to the high voltage side (HVS).

Based on these three considerations, the overall topology of the proposed converter can be shown in Fig. 4, where the left port is HVS and the right port is LVS. According to the connection way of the resonant capacitor and inductors, this converter can be named as an LLCL converter.
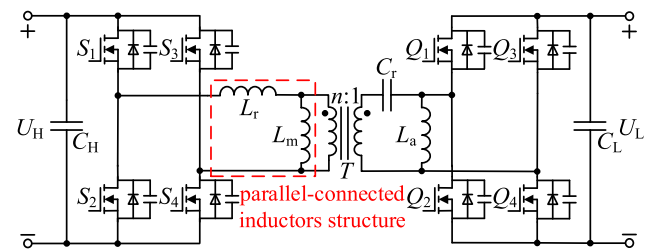

FIGURE 4. Overall topology of the proposed LLCL converter.

B. OPERATING PRINCIPLES

According to Section II-A, it can be found that LLCL can be regarded as an LLC-type IBDC. Consequently, PFM control is adopted in this paper. When the switching frequency f_S is lower than the converter's main resonant frequency, the output current of the resonant tank will cause LLCL to operate in

the discontinuous conduction mode (DCM), otherwise LLCL will work in the continuous conduction mode (CCM). Thus, operating principles of LLCL will be analyzed from forward mode and backward mode according to DCM and CCM.

1) FORWARD MODE

In this mode, power is transmitted from HVS to LVS. The key waveforms are shown in Fig. 5 based on DCM and CCM. In DCM, there are 8 intervals in a complete switching period. And the first 4 intervals are symmetric with the last 4 intervals. In CCM, 6 intervals can be demonstrated in a switching period. And the first 3 intervals are symmetric with the last 3 intervals. Since the first 3 intervals in CCM is consistent with the first 3 intervals in DCM, to simplify the analysis, only the first 4 intervals in DCM are analyzed in this paper. i_{Cr_F}, i_{La_F}, i_{Lm_F}, i_{Lr_F}, and u_{Lr_F} represent the currents flowing through C_r, L_a, L_m, L_r, and the voltage across L_r in forward mode, respectively.
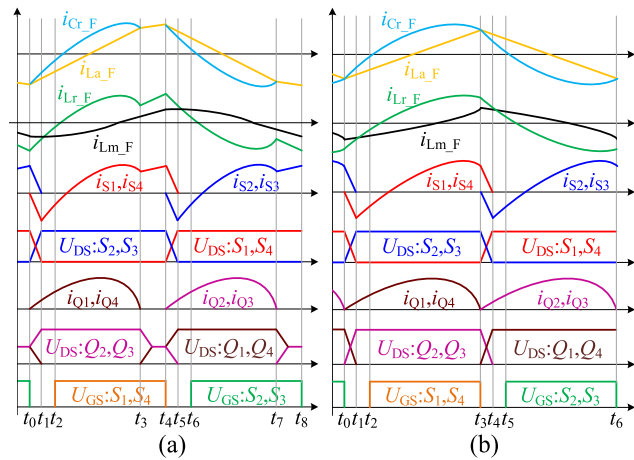

FIGURE 5. Key waveforms in forward mode. (a) DCM, (b) CCM.

a: INTERVAL 1 [t_0-t_1, Fig. 6(a)]
At t_0, S_2 and S_3 are turned OFF. Since the current through L_r cannot be mutated, the current flowing through S_2 and S_3 turns to flow through the parasitic capacitors $C_{S1} \sim C_{S4}$ of $S_1 \sim S_4$. C_{S2} and C_{S3} are charged whereas C_{S1} and C_{S4} are discharged. This interval ends at t_1 when the voltages of C_{S2} and C_{S3} rise to U_H while the voltages across C_{S1} and C_{S4} drop to zero.

b: INTERVAL 2 [t_1-t_2, Fig. 6(b)]
At t_1, since the voltages across C_{S1} and C_{S4} drop to zero, the current through L_r begins to flow through the body diodes D_{S1} and D_{S4} of S_1 and S_4, thereby creating a ZVS condition for S_1 and S_4 at t_2.

c: INTERVAL 3 [t_2-t_3, Fig. 6(c)]
At t_2, S_1 and S_4 are turned ON with ZVS. Since the MOS-switches have smaller ON-resistances than those of the
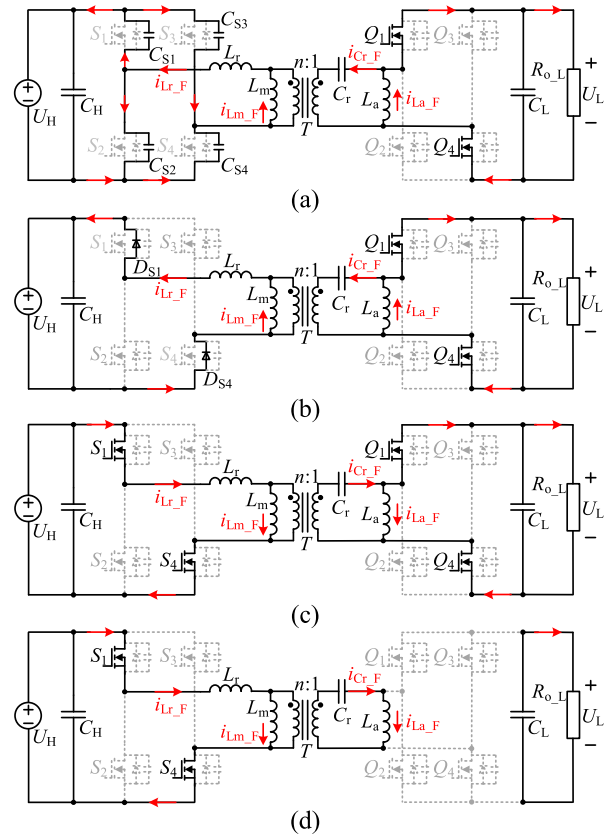

FIGURE 6. Corresponding equivalent circuits in forward mode. (a) Interval 1, (b) Interval 2, (c) Interval 3, (d) Interval 4.

diodes, the current through L_r begins to flow through S_1 and S_4 instead of D_{S1} and D_{S4}. During interval 1 to interval 3, currents and voltages of the resonant components resonate at the main resonant frequency. By the synchronous rectification, power is always transmitted to the load R_{o_L} through Q_1 and Q_4. And L_a is always forward-charged by U_L. But, since interval 1 and interval 2 are dead time durations, interval 3 becomes the main stage of the power transmission and ends until i_{Cr_F} and i_{La_F} are equal at t_3. The relation among currents and voltages of the resonant components in interval 3 can be given as:

$$\begin{cases} i_{Cr\_F}(t) = C_r \dfrac{d}{dt}[\dfrac{U_H - u_{Lr\_F}(t) - nU_L}{n}] \\ U_L = L_a \dfrac{d}{dt} i_{La\_F}(t), \quad u_{Lr\_F}(t) = L_r \dfrac{d}{dt} i_{Lr\_F}(t) \\ U_H - u_{Lr\_F}(t) = L_m \dfrac{d}{dt}[i_{Lr\_F}(t) - \dfrac{1}{n} i_{Cr\_F}(t)]. \end{cases} \quad (1)$$

According to the previous discussion of the equivalent resonant inductance L_{eq} in Section II-A, considering the influence of the transformer turns-ratio n, the main resonant frequency f_{r1_F} in forward mode can be shown as:

$$f_{r1\_F} = \frac{n}{2\pi} \sqrt{\frac{L_m + L_r}{C_r L_m L_r}}. \quad (2)$$

d: INTERVAL 4 [t_3-t_4, Fig. 6(d)]

In this interval, S_1 and S_4 are still ON. Since i_{Cr_F} and i_{La_F} are equal at t_3, the current through Q_1 and Q_4 decreases to zero. Thus, Q_1 and Q_4 are turned OFF under zero current condition. L_a is no longer charged by U_L. Power is no longer transmitted to the load. This interval is maintained until t_4 when S_1 and S_4 are turned OFF. Also, due to the fact that L_a is not controlled by U_L, L_a participates in the resonant process. The equivalent resonant inductance in this interval is L_r paralleled with L_m, and then in series with L_a. Therefore, the converter resonates at the secondary resonant frequency f_{r2_F} in this interval. f_{r2_F} can be expressed as:

$$f_{r2\_F} = \frac{n}{2\pi} \sqrt{\frac{L_m + L_r}{C_r(n^2 L_a L_m + n^2 L_a L_r + L_m L_r)}}. \quad (3)$$

2) BACKWARD MODE

In this mode, power is transmitted from LVS to HVS. The key waveforms in DCM and CCM are shown in Fig. 7. It is clearly seen that the relation between DCM and CCM in backward mode is similar to that of forward mode. Thus, to simplify the analysis, only the first 4 intervals in DCM are analyzed. i_{Cr_B}, i_{La_B}, i_{Lm_B}, i_{Lr_B}, and u_{Lm_B} represent the currents flowing through C_r, L_a, L_m, L_r, and the voltage across L_m in backward mode, respectively.
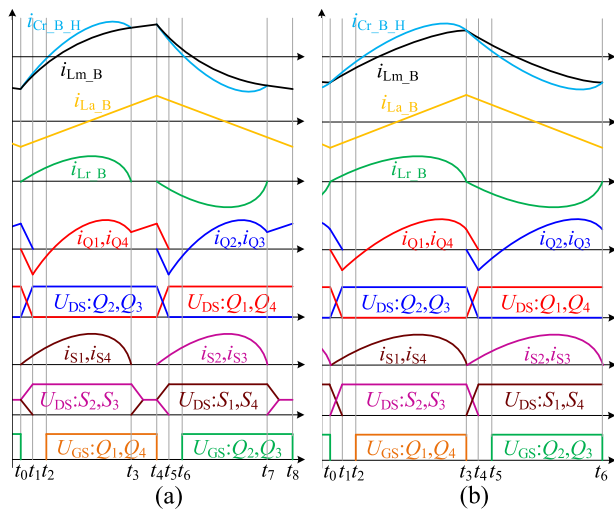

FIGURE 7. Key waveforms in backward mode. (a) DCM, (b) CCM.

a: INTERVAL 1 [t_0-t_1, Fig. 8(a)]

At t_0, Q_2 and Q_3 are turned OFF. Since i_{Cr_B} is related to i_{Lm_B} and i_{Lr_B}, i_{Cr_B} and i_{La_B} that cannot mutate make the current flowing through Q_2 and Q_3 turn to flow through the parasitic capacitors $C_{Q1} \sim C_{Q4}$ of $Q_1 \sim Q_4$. The parasitic capacitors charging and discharging processes are similar to $C_{S1} \sim C_{S4}$ in forward mode.
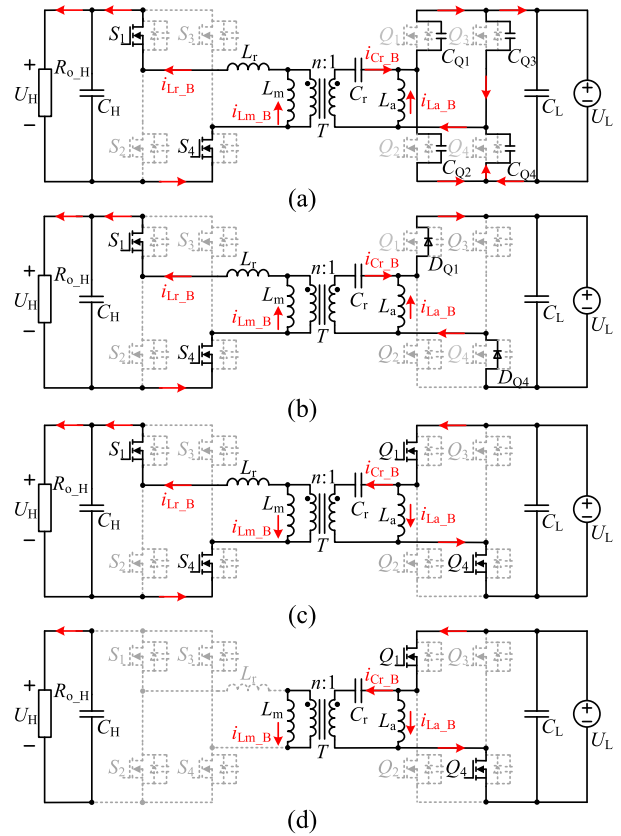

FIGURE 8. Corresponding equivalent circuits in backward mode. (a) Interval 1, (b) Interval 2, (c) Interval 3, (d) Interval 4.

b: INTERVAL 2 [t_1-t_2, Fig. 8(b)]

At t_1, since the voltages across C_{Q1} and C_{Q4} drop to zero, the sum of i_{Cr_B} and i_{La_B} begins to flow through the body diodes D_{Q1} and D_{Q4} of Q_1 and Q_4, thereby creating a ZVS condition for Q_1 and Q_4 at t_2. L_a is forward-charged by U_L.

c: INTERVAL 3 [t_2-t_3, Fig. 8(c)]

At t_2, Q_1 and Q_4 are turned ON with ZVS. The sum of i_{Cr_B} and i_{La_B} flows to Q_1 and Q_4. L_a is forward-charged by U_L. During interval 1 to interval 3, currents and voltages of the resonant components resonate at the main resonant frequency, and power is always transmitted to the load R_{o_H} through S_1 and S_4. But, since interval 1 and interval 2 are dead time durations, interval 3 becomes the main stage of power transmission and ends until $i_{Cr\_B\_H}$ (the value converted to HVS by i_{Cr_B}) and i_{Lm_B} are equal at t_3. The relation among currents and voltages of the resonant components in interval 3 can be expressed as:

$$\begin{cases} i_{Cr\_B}(t) = C_r \dfrac{d}{dt}[\dfrac{nU_L - u_{Lm\_B}(t)}{n}] \\[2mm] U_L = L_a \dfrac{d}{dt}i_{La\_B}(t), \quad u_{Lm\_B}(t) = L_m \dfrac{d}{dt}i_{Lm\_B}(t) \\[2mm] u_{Lm\_B}(t) - U_H = L_r \dfrac{d}{dt}[\dfrac{1}{n}i_{Cr\_B}(t) - i_{Lm\_B}(t)]. \end{cases} \quad (4)$$

According to the analysis in Section II-A, at the stage where power can be transmitted, L_{eq} will be the same in forward and backward modes. Thus, the main resonant frequency f_{r1_B} in backward mode is the same with f_{r1_F}. For simplification, the main resonant frequency in both forward and backward modes can be collectively referred to as f_{r1}.

d: INTERVAL 4 [t_3-t_4, Fig. 8(d)]
In this interval, Q_1 and Q_4 are still ON, so L_a is still charged by U_L. Since $i_{Cr\_B\_H}$ and i_{Lm_B} are equal at t_3, the current through S_1 and S_4 decreases to zero. As a result, S_1 and S_4 are turned OFF under zero current condition. Power is no longer transmitted to the load. This interval is maintained until t_4 when Q_1 and Q_4 are turned OFF. Also, since there is no current through L_r, currents and voltages of C_r and L_m resonate at the secondary resonant frequency f_{r2_B} in this interval. f_{r2_B} can be given as:

$$f_{r2\_B} = \frac{n}{2\pi}\sqrt{\frac{1}{C_r L_m}}. \tag{5}$$

III. CHARACTERISTICS ANALYSES
A. DC VOLTAGE GAIN ANALYSIS
For gain analysis, the fundamental harmonic approximation (FHA) method is adopted in this paper. Fig. 9 shows the FHA equivalent circuits of LLCL in forward and backward modes. E_{iF}, E_{oF}, and R_{eq_L} are the input voltage, output voltage and equivalent ac load resistance, respectively, of the resonant tank in forward mode, whereas E_{iB}, E_{oB}, and R_{eq_H} are the corresponding meanings in backward mode. Expressions of R_{eq_L} and R_{eq_H} are given in (6), as shown at the bottom of the page, according to [25]. Meanwhile, the equivalent resonant capacitance C_{eq}, equivalent resonant inductance L_{eq}, inductance ratios k and g, normalized switching frequency f_n, and quality factor in forward mode (Q_F) and backward mode (Q_B) are also given or defined in (6). By means of (2), (6), Fig. 9, and Kirchhoff's current/voltage laws, the dc voltage gain of LLCL in forward mode (M_F) and backward mode (M_B) can be deduced as (7) and (8), as shown at the bottom of the page, respectively.

Based on (7) and (8), curves of M_F and M_B are presented in Fig. 10. When LLCL operates near the main resonant
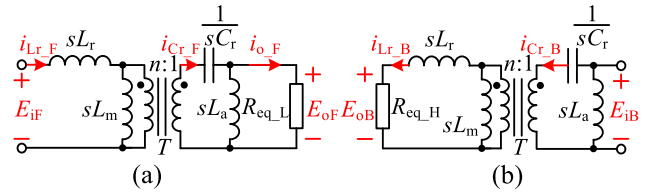

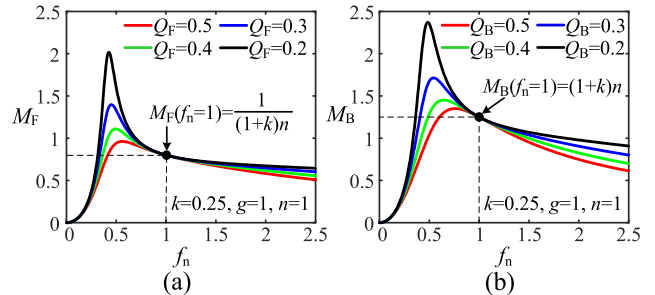**FIGURE 9.** FHA equivalent circuits of LLCL converter. (a) Forward mode, (b) Backward mode.

FIGURE 10. DC voltage gain curves of LLCL converter. (a) Forward mode, (b) Backward mode.

frequency f_{r1} (i.e., f_n is around 1), it can be seen that M_F and M_B both gradually decrease as f_n increases, which means the voltage gain can be effectively regulated by regulating the switching frequency f_S. Meanwhile, M_F and M_B are exactly the reciprocal of each other when $f_n = 1$, which is benefit for matching U_H and U_L. Moreover, when f_n is slightly lower than 1, not only M_F but also M_B can rise as f_n reduces, which is also a major improvement over conventional LLC-type converters in bidirectional applications.

B. RESONANT TANK ANALYSIS
To simplify the analysis, the switching dead time is ignored in this section. Therefore, when LLCL operates at the main resonant frequency, according to Fig. 6(c) and Fig. 8(c), some extra equations in forward mode and backward mode can be obtained and shown in (9) and (10), as shown at the bottom of the next page, respectively, where T_S is the switching period.

By combining (1), (4), (9), and (10), current and voltage expressions in LLCL resonant tank can be obtained. Since LLCL is derived from Bi-LLC, to demonstrate the effect

$$\begin{cases} R_{eq\_L} = \frac{8}{\pi^2}R_{o\_L}, R_{eq\_H} = \frac{8}{\pi^2}R_{o\_H}, C_{eq} = \frac{C_r}{n^2}, L_{eq} = \frac{L_m L_r}{L_m + L_r} \\ k = \frac{L_r}{L_m}, g = \frac{L_a}{L_m}, f_n = \frac{f_S}{f_{r1}}, Q_F = \frac{\sqrt{L_{eq}/C_{eq}}}{n^2 R_{eq\_L}}, Q_B = \frac{\sqrt{L_{eq}/C_{eq}}}{R_{eq\_H}} \end{cases} \tag{6}$$

$$M_F = \frac{U_L}{U_H} = \left| \frac{(\pi/2\sqrt{2})E_{oF}}{(\pi/2\sqrt{2})E_{iF}} \right| = \frac{1}{\sqrt{[\frac{k}{gn}(1 - \frac{1}{f_n^2}) + (1+k)n]^2 + Q_F^2(f_n - \frac{1}{f_n})^2(1+k)^2 n^2}} \tag{7}$$

$$M_B = \frac{U_H}{U_L} = \left| \frac{(\pi/2\sqrt{2})E_{oB}}{(\pi/2\sqrt{2})E_{iB}} \right| = \frac{1}{\sqrt{[\frac{1}{n} - \frac{k}{f_n^2(1+k)n}]^2 + Q_B^2(f_n - \frac{1}{f_n})^2(1+k)^2 \frac{1}{n^2}}} \tag{8}$$

of LLCL in reducing the resonant tank currents and the resonant capacitor voltage stress, Bi-LLC shown in Fig. 2(a) will be analyzed as a comparative topology in this section. Meanwhile, according to (7) and (8), it can be observed that the voltage gain of LLCL is directly affected by the transformer turns-ratio, quality factor, and the resonant inductance ratios, which is similar to the other LLC-type resonant converters. Hence, these variables that reflect the converters' working conditions will be considered in the comparisons. To eliminate the side effects of the transformer turns-ratio, $n = 1$ is adopted for both converters in current and voltage comparisons.

1) INPUT AND OUTPUT CURRENTS OF THE RESONANT TANK

With regard to the resonant tank, since its input and output current are equal to the current through the inverter switches and rectifier switches, respectively, these currents will ultimately affect the switch conduction losses. Therefore, analysis of the resonant tank's input root-mean-square (RMS) current (IRMSC) and output RMS current (ORMSC) is very important. For LLCL, according to (1), (4), (9), and (10), time domain expressions of the resonant tank's input

current ($i_{\text{in\_F}}(t)$ in forward mode, $i_{\text{in\_B}}(t)$ in backward mode) and output current ($i_{\text{out\_F}}(t)$ in forward mode, $i_{\text{out\_B}}(t)$ in backward mode) can be totally given in (11), as shown at the bottom of the page. Based on (11) and the variables announced in (6), by taking the dc output current as the base value, the normalized IRMSC I_{in}(norm) and the normalized ORMSC I_{out}(norm) can be given by (12), as shown at the bottom of the page. The intermediate variables $A \sim F$ in (12) are listed in Table 1. By choosing the same base value, the normalized IRMSC I_{in}(norm) and ORMSC I_{out}(norm) of Bi-LLC can also be given by (12). For intermediate variables $A \sim F$ fit for Bi-LLC under $n = 1$, they are also given in Table 1 for further comparison (time domain expressions of $i_{\text{in\_F}}(t)$, $i_{\text{in\_B}}(t)$, $i_{\text{out\_F}}(t)$, and $i_{\text{out\_B}}(t)$ of Bi-LLC are given in the appendix).

Based on (12) and Table 1, when $n = 1$ and $g = 1$, the normalized IRMSC and ORMSC comparison results between LLCL and Bi-LLC are illustrated in Fig. 11. As seen in Fig. 11(a) and (c), LLCL has lower IRMSC and lower ORMSC over wide ranges of k and Q_{F} in forward mode. When backward mode is applied, it is clearly seen from Fig. 11(d) that the ORMSC of LLCL is always lower than that of Bi-LLC. For IRMSC, as noticed in Fig. 11(b),

$$
\begin{cases}
i_{\text{Cr\_F}}(0) = i_{\text{La\_F}}(0), \; i_{\text{La\_F}}(0) = -i_{\text{La\_F}}(\dfrac{T_{\text{S}}}{2}) \\[2mm]
i_{\text{Lm\_F}}(0) = -i_{\text{Lm\_F}}(\dfrac{T_{\text{S}}}{2}), \; \dfrac{2}{T_{\text{S}}} \displaystyle\int_{0}^{\frac{T_{\text{S}}}{2}} [i_{\text{Cr\_F}}(t) - i_{\text{La\_F}}(t)]\mathrm{d}t = \dfrac{U_{\text{L}}}{R_{\text{o\_L}}}
\end{cases} \tag{9}
$$

$$
\begin{cases}
i_{\text{Cr\_B}}(0) = ni_{\text{Lm\_B}}(0), \; i_{\text{La\_B}}(0) = -i_{\text{La\_B}}(\dfrac{T_{\text{S}}}{2}) \\[2mm]
i_{\text{Lm\_B}}(0) = -i_{\text{Lm\_B}}(\dfrac{T_{\text{S}}}{2}), \; \dfrac{2}{T_{\text{S}}} \displaystyle\int_{0}^{\frac{T_{\text{S}}}{2}} [\dfrac{i_{\text{Cr\_B}}(t)}{n} - i_{\text{Lm\_B}}(t)]\mathrm{d}t = \dfrac{U_{\text{H}}}{R_{\text{o\_H}}}
\end{cases} \tag{10}
$$

$$
\begin{cases}
i_{\text{in\_F}}(t) = \dfrac{4U_{\text{L}}}{(1+k)\pi n R_{\text{eq\_L}}} \sin \omega_{\text{r}} t - \dfrac{k\pi U_{\text{L}}}{2g(1+k)^2 n^3 Q_{\text{F}} R_{\text{eq\_L}}} \cos \omega_{\text{r}} t \\[2mm]
\quad + \dfrac{kU_{\text{L}}}{(1+k)n Q_{\text{F}} R_{\text{eq\_L}}} \omega_{\text{r}} t - \dfrac{k\pi U_{\text{L}}}{2(1+k)n Q_{\text{F}} R_{\text{eq\_L}}} \\[2mm]
i_{\text{in\_B}}(t) = \dfrac{4(1+k)n U_{\text{H}}}{\pi R_{\text{eq\_H}}} \sin \omega_{\text{r}} t - \dfrac{k\pi n U_{\text{H}}}{2(1+k) Q_{\text{B}} R_{\text{eq\_H}}} \cos \omega_{\text{r}} t \\[2mm]
\quad + \dfrac{kU_{\text{H}}}{g(1+k)^2 n Q_{\text{B}} R_{\text{eq\_H}}} \omega_{\text{r}} t - \dfrac{k\pi U_{\text{H}}}{2g(1+k)^2 n Q_{\text{B}} R_{\text{eq\_H}}} \\[2mm]
i_{\text{out\_F}}(t) = \dfrac{4U_{\text{L}}}{\pi R_{\text{eq\_L}}} \sin \omega_{\text{r}} t - \dfrac{k\pi U_{\text{L}}}{2g(1+k)n^2 Q_{\text{F}} R_{\text{eq\_L}}} \cos \omega_{\text{r}} t \\[2mm]
\quad - \dfrac{kU_{\text{L}}}{g(1+k)n^2 Q_{\text{F}} R_{\text{eq\_L}}} \omega_{\text{r}} t + \dfrac{k\pi U_{\text{L}}}{2g(1+k)n^2 Q_{\text{F}} R_{\text{eq\_L}}} \\[2mm]
i_{\text{out\_B}}(t) = \dfrac{4U_{\text{H}}}{\pi R_{\text{eq\_H}}} \sin \omega_{\text{r}} t - \dfrac{k\pi U_{\text{H}}}{2(1+k)^2 Q_{\text{B}} R_{\text{eq\_H}}} \cos \omega_{\text{r}} t \\[2mm]
\quad - \dfrac{kU_{\text{H}}}{(1+k)^2 Q_{\text{B}} R_{\text{eq\_H}}} \omega_{\text{r}} t + \dfrac{k\pi U_{\text{H}}}{2(1+k)^2 Q_{\text{B}} R_{\text{eq\_H}}}
\end{cases} \tag{11}
$$

$$
\begin{cases}
I_{\text{in}}(\text{norm}) = \sqrt{\dfrac{6\pi A^2 + 6\pi B^2 + 48BC + \pi^3 C^2}{12\pi}} \\[3mm]
I_{\text{out}}(\text{norm}) = \sqrt{\dfrac{6\pi D^2 + 6\pi E^2 + 48EF + \pi^3 F^2}{12\pi}}
\end{cases} \tag{12}
$$

TABLE 1. Intermediate variables in (12).

	Forward mode	Backward mode
LLCL	$A = \dfrac{\pi}{2(1+k)n}, B = \dfrac{k\pi^3}{16g(1+k)^2n^3Q_F}, C = \dfrac{k\pi^2}{8(1+k)nQ_F}$ $D = \dfrac{\pi}{2}, E = \dfrac{k\pi^3}{16g(1+k)n^2Q_F}, F = -\dfrac{k\pi^2}{8g(1+k)n^2Q_F}$	$A = \dfrac{(1+k)n\pi}{2}, B = \dfrac{kn\pi^3}{16(1+k)Q_B}, C = \dfrac{k\pi^2}{8g(1+k)^2nQ_B}$ $D = \dfrac{\pi}{2}, E = \dfrac{k\pi^3}{16(1+k)^2Q_B}, F = -\dfrac{k\pi^2}{8(1+k)^2Q_B}$
Bi-LLC ($n=1$)	$A = D = \dfrac{\pi}{2}, B = E = \dfrac{k\pi^3}{16gQ_F}, C = \dfrac{k\pi^2}{8Q_F}, F = -\dfrac{k\pi^2}{8gQ_F}$	$A = D = \dfrac{\pi}{2}, B = E = \dfrac{k\pi^3}{16Q_B}, C = \dfrac{k\pi^2}{8gQ_B}, F = -\dfrac{k\pi^2}{8Q_B}$

TABLE 2. Normalized turn-off current expressions.

	Forward mode	Backward mode
LLCL	$\dfrac{k\pi^3[g(1+k)n^2+1]}{16g(1+k)^2n^3Q_F}$	$\dfrac{k\pi^3[g(1+k)n^2+1]}{16g(1+k)^2nQ_B}$
Bi-LLC ($n=1$)	$\dfrac{k\pi^3(g+1)}{16gQ_F}$	$\dfrac{k\pi^3(g+1)}{16gQ_B}$

although the value of LLCL is higher than that of Bi-LLC when k is low and Q_B is high, the IRMSC value difference is quite small in these cases. Thus, performance difference can be ignored. However, as k increases and Q_B decreases, lower IRMSC will still become more and more apparent in LLCL. Consequently, in the case of wide k and wide load (Q_F or Q_B) conditions, compared with Bi-LLC, LLCL has obvious advantages in reducing IRMSC and ORMSC, which is benefit for improving efficiency.

Also, according to [30], for an inverter power switch, the relation between its turn-off loss P_{off} and turn-off current i_{off} can be given in (13), where U_{ds} is its drain-source voltage and T_{off} is its turn-off time. It means the turn-off loss and the turn-off current have a positive correlation when U_{ds}, T_{off}, and f_S are all the same. Thus, it is meaningful to reduce the turn-off current of the inverter switch. Based on (10), when t is equal to the half switching period $T_S/2$, turn-off current i_{off_F} of LLCL's inverter switch in forward mode can be calculated by $i_{in\_F}(t)$. Similarly, turn-off current i_{off_B} of the inverter switch in backward mode can be calculated by $i_{in\_B}(t)$. The results of i_{off_F} and i_{off_B} are shown in (14).

$$P_{off} = \frac{1}{6}U_{ds}i_{off}T_{off}f_S \tag{13}$$

$$\begin{cases} i_{off\_F} = i_{in\_F}\left(\dfrac{T_S}{2}\right) = \dfrac{k\pi U_L[g(1+k)n^2+1]}{2g(1+k)^2n^3Q_FR_{eq\_L}} \\ i_{off\_B} = i_{in\_B}\left(\dfrac{T_S}{2}\right) = \dfrac{k\pi U_H[g(1+k)n^2+1]}{2g(1+k)^2nQ_BR_{eq\_H}} \end{cases} \tag{14}$$

When the dc output current is taken as the base value, the normalized inverter switch turn-off current I_{off}(norm) of LLCL in forward and backward modes can be given in Table 2. By combining the expressions of i_{off_F} and i_{off_B}
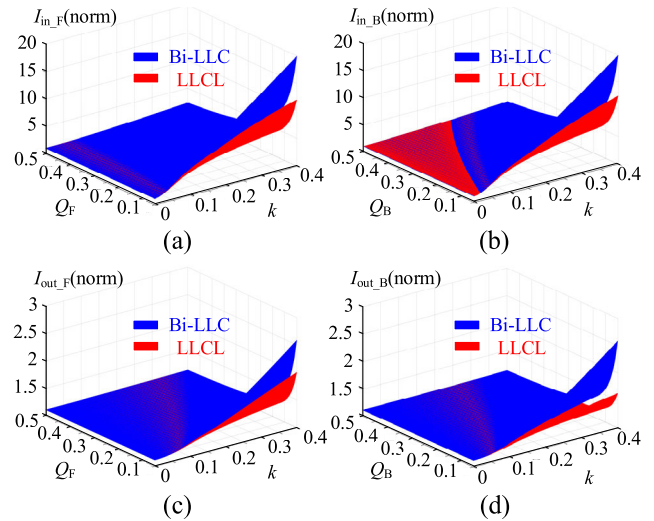

FIGURE 11. Normalized IRMSC and ORMSC comparisons between LLCL and Bi-LLC. (a) IRMSC, forward mode, (b) IRMSC, backward mode, (c) ORMSC, forward mode, (d) ORMSC, backward mode.
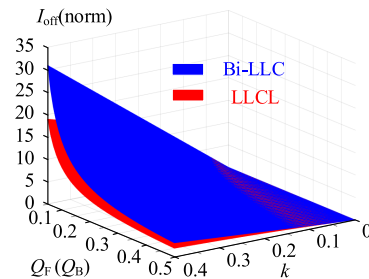

FIGURE 12. Normalized inverter switch turn-off current comparison between LLCL and Bi-LLC in both forward and backward modes.

of Bi-LLC given in the appendix, I_{off}(norm) of Bi-LLC under $n = 1$ are also shown in Table 2 for the comparison.

From Table 2, it can be noticed that the normalized turn-off current values in forward mode and backward mode are the same when $n = 1$, so the comparison between LLCL and Bi-LLC in both forward and backward modes can be shown in a single figure (Fig. 12). The comparison result under $n = 1$ and $g = 1$ verifies that LLCL has lower turn-off current than Bi-LLC over wide ranges of k and quality factor (Q_F and Q_B), which means LLCL has obvious potential to reduce the switch turn-off losses.

TABLE 3. Intermediate variables in (17) and (18).

	Forward mode	Backward mode
LLCL in (17)	$a = \dfrac{k\pi^2}{8g(1+k)n^2Q_F}, b = \dfrac{\pi}{2(1+k)n}, c = \dfrac{k\pi^3}{16g(1+k)^2n^3Q_F}, d = \dfrac{k\pi^2}{8(1+k)nQ_F}$	$a = \dfrac{k\pi^2}{8g(1+k)^2nQ_B}, b = \dfrac{\pi}{2}, c = \dfrac{k\pi^3}{16(1+k)^2Q_B}, d = -\dfrac{k\pi^2}{8(1+k)^2Q_B}$
Bi-LLC in (18) (n=1)	$a = \dfrac{k\pi^2}{8gQ_F}, b = \dfrac{k\pi^2}{8Q_F}, c = \dfrac{\pi}{2}, d = \dfrac{k\pi^3}{16gQ_F}$	$a = \dfrac{k\pi^2}{8gQ_B}, b = \dfrac{k\pi^2}{8Q_B}, c = \dfrac{\pi}{2}, d = \dfrac{k\pi^3}{16Q_B}$

2) CURRENTS AND VOLTAGES OF THE RESONANT COMPONENTS

As for the resonant inductors, their winding equivalent ac resistances will generate winding losses. For the resonant capacitor, on one hand, voltage stress is an important consideration that determine the capacitor cost and reliability. On the other hand, the capacitor losses are generally composed of the dielectric losses P_d [29], whose relation with the peak-to-peak voltage U_{Cr_pp} of capacitor C_r can be shown in (15). It means that the capacitor losses are generally related to the voltage stress of the capacitor. Thus, it is necessary to reduce the RMS currents through the resonant inductors and the voltage stress of the resonant capacitor.

$$P_d = C_r U_{Cr\_pp} f_S \tan \delta \qquad (15)$$

where $\tan\delta$ is the capacitor dielectric loss factor.

For LLCL converter, the current through L_a ($i_{La\_F}(t)$ in forward mode, $i_{La\_B}(t)$ in backward mode), L_m ($i_{Lm\_F}(t)$ in forward mode, $i_{Lm\_B}(t)$ in backward mode), and L_r ($i_{Lr\_F}(t)$ in forward mode, $i_{Lr\_B}(t)$ in backward mode) are all given in (16), as shown at the bottom of the page. Based on (16), by taking the dc output current as the base value, the corresponding normalized RMS currents $I_{La}(norm)$, $I_{Lm}(norm)$, and $I_{Lr}(norm)$ can be derived as (17), as shown at the bottom of the page. The intermediate variables $a \sim d$ in (17) are listed in Table 3. According to the same base value, $I_{La}(norm)$, $I_{Lm}(norm)$, and $I_{Lr}(norm)$ of Bi-LLC can be given in (18), as shown at the bottom of the page. Its intermediate variables $a \sim d$ under $n = 1$ are also listed in Table 3 so as to make the comparison ($i_{La\_F}(t)$, $i_{La\_B}(t)$, $i_{Lm\_F}(t)$, $i_{Lm\_B}(t)$, $i_{Lr\_F}(t)$, and $i_{Lr\_B}(t)$ of Bi-LLC are given in the appendix).

By combining (17), (18), and Table 3, when $n = 1$ and $g = 1$, the resonant inductors' normalized RMS current comparisons between LLCL and Bi-LLC in forward and backward modes can be totally shown in Fig. 13. As can be seen, although in some cases, the inductor RMS current

$$
\begin{cases}
i_{La\_F}(t) = \dfrac{kU_L}{g(1+k)n^2Q_FR_{eq\_L}}\omega_r t - \dfrac{k\pi U_L}{2g(1+k)n^2Q_FR_{eq\_L}} \\[2mm]
i_{La\_B}(t) = \dfrac{kU_H}{g(1+k)^2nQ_BR_{eq\_H}}\omega_r t - \dfrac{k\pi U_H}{2g(1+k)^2nQ_BR_{eq\_H}} \\[2mm]
i_{Lm\_F}(t) = \dfrac{-4kU_L}{(1+k)\pi nR_{eq\_L}}\sin\omega_r t + \dfrac{k^2\pi U_L}{2g(1+k)^2n^3Q_FR_{eq\_L}}\cos\omega_r t \\[2mm]
\qquad\qquad + \dfrac{kU_L}{(1+k)nQ_FR_{eq\_L}}\omega_r t - \dfrac{k\pi U_L}{2(1+k)nQ_FR_{eq\_L}} \\[2mm]
i_{Lm\_B}(t) = \dfrac{4kU_H}{\pi R_{eq\_H}}\sin\omega_r t - \dfrac{k^2\pi U_H}{2(1+k)^2Q_BR_{eq\_H}}\cos\omega_r t \\[2mm]
\qquad\qquad + \dfrac{kU_H}{(1+k)^2Q_BR_{eq\_H}}\omega_r t - \dfrac{k\pi U_H}{2(1+k)^2Q_BR_{eq\_H}} \\[2mm]
i_{Lr\_F}(t) = i_{in\_F}(t), \ i_{Lr\_B}(t) = i_{out\_B}(t)
\end{cases} \qquad (16)
$$

$$
\text{LLCL}: \begin{cases}
I_{La}(norm) = \dfrac{\pi a}{\sqrt{12}} \\[3mm]
I_{Lm}(norm) = \sqrt{\dfrac{6\pi k^2 b^2 + 6\pi k^2 c^2 - 48kcd + \pi^3 d^2}{12\pi}} \\[4mm]
I_{Lr}(norm) = \sqrt{\dfrac{6\pi b^2 + 6\pi c^2 + 48cd + \pi^3 d^2}{12\pi}}
\end{cases} \qquad (17)
$$

$$
\text{Bi-LLC}: \begin{cases}
I_{La}(norm) = \dfrac{\pi a}{\sqrt{12}}, \quad I_{Lm}(norm) = \dfrac{\pi b}{\sqrt{12}} \\[3mm]
I_{Lr}(norm) = \sqrt{\dfrac{c^2 + d^2}{2}}
\end{cases} \qquad (18)
$$

values of LLCL are greater than the corresponding values of Bi-LLC, the values difference of the two converters in these cases are all so small, so performance difference can be ignored. However, when the current values difference between the two converters is obvious, LLCL can always obtain a lower value than that of Bi-LLC. As a result, higher efficiency will be achieved in LLCL due to the lower winding losses.

Also, for LLCL, the resonant capacitor voltage expressions ($u_{Cr\_F}(t)$ in forward mode, $u_{Cr\_B}(t)$ in backward mode) can be given in (19). Based on (19), the peak voltage of the resonant capacitor (voltage stress) can be obtained easily. By selecting the dc output voltage as the base value, the normalized voltage stresses ($U_{Cr\_F}(norm)$ in forward mode and $U_{Cr\_B}(norm)$ in backward mode) can be calculated and shown in Table 4. For comparison, $U_{Cr\_F}(norm)$ and $U_{Cr\_B}(norm)$ of Bi-LLC under $n = 1$ are also listed ($u_{Cr\_F}(t)$ and $u_{Cr\_B}(t)$ of Bi-LLC are given in the appendix).

$$
\begin{cases}
u_{Cr\_F}(t) = \dfrac{-k\pi U_L}{2g(1+k)n^2}\left[\dfrac{8g(1+k)n^2 Q_F}{k\pi^2}\cos\omega_r t + \sin\omega_r t\right] \\
u_{Cr\_B}(t) = \dfrac{-k\pi U_H}{2(1+k)n}\left[\dfrac{8(1+k)^2 Q_B}{k\pi^2}\cos\omega_r t + \sin\omega_r t\right]
\end{cases}
$$

$$(19)$$

TABLE 4. Normalized resonant capacitor voltage stress expressions.

	Forward mode	Backward mode
LLCL	$\dfrac{k\pi}{2g(1+k)n^2}\times$ $\sqrt{\dfrac{64g^2(1+k)^2 n^4 Q_F^2}{k^2\pi^4}+1}$	$\dfrac{k\pi}{2(1+k)n}\times$ $\sqrt{\dfrac{64(1+k)^4 Q_B^2}{k^2\pi^4}+1}$
Bi-LLC (n=1)	$\dfrac{k\pi}{2g}\sqrt{\dfrac{64g^2 Q_F^2}{k^2\pi^4}+1}$	$\dfrac{k\pi}{2}\sqrt{\dfrac{64Q_B^2}{k^2\pi^4}+1}$

Based on Table 4, Fig. 14 shows the normalized resonant capacitor voltage stress comparison results between LLCL and Bi-LLC in both modes when $n = 1$ and $g = 1$. It can be seen that LLCL always has a lower voltage stress in forward mode. In backward mode, since the too small inductance ratio k will limit the voltage boost capability of the LLC-type resonant converters [31], LLCL will also obtain lower voltage stress over a reasonable selection range of k, especially under light load (light Q_B) conditions.

At last, it should be noted that all of the above comparison results have similar characteristics when g is taken other reasonable values. Hence, the comparison results under other g are no longer given to save space.

C. COMPARISONS WITH CLLC

For CLLC shown in Fig. 2(b), three Y-connected inductors can also make the converter have a parallel-connected inductors structure in bidirectional operations. However, because its overall structure has many differences with LLCL and Bi-LLC, and more resonant elements also make it difficult to
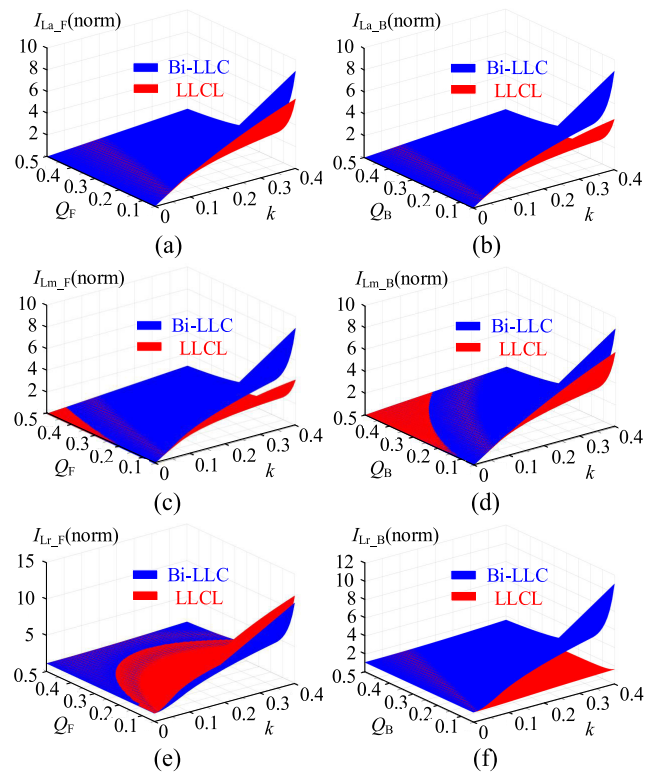

FIGURE 13. Normalized resonant inductors RMS current comparisons between LLCL and Bi-LLC. (a) Current of L_a, forward mode, (b) Current of L_a, backward mode, (c) Current of L_m, forward mode, (d) Current of L_m, backward mode, (e) Current of L_r, forward mode, (f) Current of L_r, backward mode.
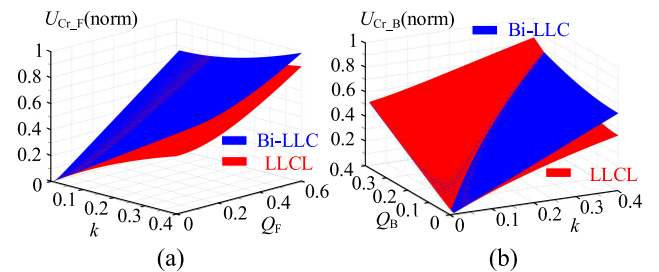

FIGURE 14. Normalized resonant capacitor voltage stress comparisons between LLCL and Bi-LLC. (a) Forward mode, (b) Backward mode.

obtain the accurate resonant current and voltage time domain expressions, CLLC has not been compared in the previous analysis. To this end, this section will use PSIM software to simulate the performance difference between LLCL and CLLC. The parameters of LLCL in the simulation are set as the experimental parameters in Section V, and CLLC is parameterized according to the same rated power, rated output voltage, quality factor, main resonant frequency, inductance ratio k, and transformer turns-ratio.

Table 5 shows the simulation results of LLCL and CLLC operating at their main resonant frequency (100kHz), rated power (500W), and rated output voltage (50V in forward mode and 200V in backward mode). Since both LLCL and

TABLE 5. Comparisons between LLCL and CLLC.

Converters	LLCL		CLLC	
Power flow mode	Forward mode	Backward mode	Forward mode	Backward mode
IRMSC (A)	4.38	16.44	5.56	17.84
ORMSC (A)	10.83	2.70	10.84	2.72
Inverter switch turn-off current (A)	5.39	19.41	6.54	24.05
RMS current of inductor-1 (A)	4.38	2.70	5.56	2.72
RMS current of inductor-2 (A)	5.82	5.84	10.84	17.84
RMS current of inductor-3 (A)	1.42	2.40	3.93	5.23
Resonant capacitor voltage stresses (V)	43.13	42.33	94.71 21.05	47.69 32.98
Efficiency/reliability under the same working conditions	High		Low	
Resonant components amount	3 inductors 1 capacitor		3 inductors 2 capacitors	
Cost	Low		High	

CLLC have three resonant inductors, the inductors can be called as inductor-1, inductor-2, and inductor-3 for convenience. In terms of the resonant tank currents, it can be found from Table 5 that although LLCL has only a slight advantage in reducing IRMSC, ORMSC, and inverter switch turn-off current, the advantage in reducing resonant inductors RMS currents is quite obvious. It shows that although CLLC also has a parallel-connected inductors structure, the currents inside the CLLC resonant tank are still higher than those of LLCL due to the specific structure difference. In addition, for the resonant capacitor voltage stress comparisons, LLCL has lower voltage stresses in both power directions. And this advantage is particularly obvious in forward mode, which can be attributed to the fact that in order to effectively utilize the transformer magnetizing inductor, the position of the transformer will make one of the two capacitors in CLLC be inevitably placed on HVS.

In summary, owing to the lower resonant tank currents, LLCL can achieve higher efficiency than CLLC. Further, since LLCL also reduces the voltage stress and amount of the resonant capacitors, higher reliability and lower cost will also become the advantages of LLCL.

IV. PARAMETER DESIGN
A. VOLTAGE GAIN RANGE POINT OF VIEW
For LLC-type resonant converters with PFM control method, in addition to the transformer turns-ratio, their voltage gain will also be affected by the resonant inductance ratios, quality factor, and the normalized switching frequency. Therefore, the width of the voltage gain range will also be determined by the above parameters. Hence, to make LLCL have a desirable voltage gain range, three selection constraints are carried out to determine the relevant parameters step by step.

Constraint 1: Preliminary selection of k and g based on suppression of excessive resonant tank currents.

For LLC-type converters, to prevent excessive currents in the resonant tank, the inductance of the parallel inductor (such as the magnetizing inductance of conventional LLC) should not be too small [31]. Thus, for LLCL, the value relations among its series inductor (L_r) and parallel inductors (L_a and L_m) can be set as (20). By combining (6), (20) can be further organized into (21) containing k and g.

$$L_r/L_m < 0.4, \quad L_r/(n^2 L_a) < 0.4 \tag{20}$$

$$k < 0.4, \quad g > k/(0.4n^2) \tag{21}$$

Constraint 2: Maximum range of the normalized switching frequency f_n.

For LLC-type converters with PFM control method, the conversion efficiency will decrease as the switching frequency moves away from the main resonant frequency. Thus, it is best to make the switching frequency near the main resonant frequency while obtaining the desired gain range. To this end, the maximum variation range of the switching frequency in forward and backward modes are both set as $0.75f_{r1} \leq f_S \leq 1.25f_{r1}$, which means:

$$0.75 \leq f_n \leq 1.25. \tag{22}$$

Constraint 3: Voltage gain requirements.

To simulate the terminal voltage feature of the energy storage batteries connected to LVS, the rated voltage value on LVS is set to 50V and the fluctuation range is between 45V and 55V. Therefore, when the high dc bus voltage is set to 200V, the voltage gain of LLCL needs to meet the following requirements.

Constraint 3-1: Voltage gain at the main resonant frequency f_{r1}.

According to (7) and (8), when LLCL operates at the main resonant frequency f_{r1} (i.e., $f_n = 1$), it can be found that the ratio between U_H and U_L is constant at $(1+k)n$ regardless of the direction and amplitude of the transferred power. Hence, to make the voltage gain of LLCL exactly match the rated values of U_H and U_L when $f_S = f_{r1}$, set:

$$(1 + k)n = 4. \tag{23}$$

Constraint 3-2: Voltage gain range.

To make LLCL effectively match the fluctuating LVS voltage within the limited f_n range, the voltage gains M_F and M_B at the f_n boundary shown in (22) should satisfy (24). Moreover, within the entire f_n range, M_F and M_B need to decrease monotonically along with the switching frequency increment to ensure the effectiveness of PFM control.

$$\begin{cases} M_F(f_n = 0.75) > 0.275, \quad M_F(f_n = 1.25) < 0.225 \\ M_B(f_n = 0.75) > 4.45, \quad M_B(f_n = 1.25) < 3.6 \end{cases} \tag{24}$$

Meanwhile, by substituting (23) into (7) and (8), M_F and M_B can be rewritten as:

$$M_F = \frac{1}{\sqrt{[\frac{k(1+k)}{4g}(1 - \frac{1}{f_n^2}) + 4]^2 + 16Q_F^2(f_n - \frac{1}{f_n})^2}} \tag{25}$$

$$M_B = \frac{4}{\sqrt{[(1+k) - \frac{k}{f_n^2}]^2 + Q_B^2(f_n - \frac{1}{f_n})^2(1+k)^4}}. \quad (26)$$

It is clearly seen from (25) and (26) that M_F is related to k, g, Q_F, and f_n, whereas M_B is only related to k, Q_B, and f_n. Therefore, to simplify the design difficulty, the constraints on M_B can be firstly analyzed to determine the reasonable value ranges of k and Q_B.

Constraint 3-2-1: $M_B(f_n = 1.25) < 3.6$.

Fig. 15(a) is a graphic of M_B versus k and Q_B when $f_n = 1.25$. It is seen that under the same k, M_B will decrease as the load (Q_B) increases. Since this constraint limits the upper limit of M_B, attention should be paid to the light load condition. According to Fig. 15(a), it can be found that k needs to be greater than 0.31 to ensure that this constraint can still be satisfied in near no-load operation. On the other hand, to simplify the transformer design, the turns-ratio n can be taken as an integer as much as possible. Since (21) requires k to be less than 0.4, the relation between k and n shown in (23) can be combined to choose:

$$k = 0.333, \quad n = 3. \quad (27)$$

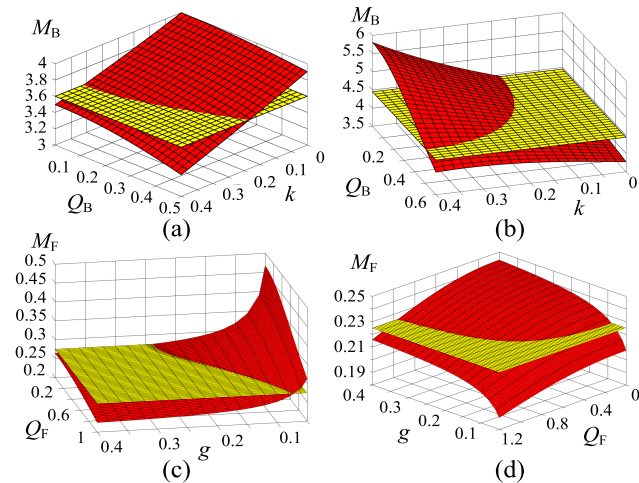M_B

(a)

M_B

(b)

M_F

(c)

M_F

(d)

FIGURE 15. 3-D relations of the voltage gain with quality factor and inductance ratio. (a) M_B versus Q_B and k under $f_n = 1.25$, (b) M_B versus Q_B and k under $f_n = 0.75$, (c) M_F versus Q_F and g under $f_n = 0.75$, (d) M_F versus Q_F and g under $f_n = 1.25$.

Constraint 3-2-2: $M_B(f_n = 0.75) > 4.45$.

Fig. 15(b) is a graphic of M_B versus k and Q_B when $f_n = 0.75$. It indicates that Q_B and M_B are also reversely correlated under the same k. Therefore, when $k = 0.333$, to ensure this constraint from light to full load operations, according to Fig. 15(b), Q_B should meet (28) at full load

$$Q_B < 0.49. \quad (28)$$

Constraint 3-2-3: $M_F(f_n = 0.75) > 0.275$.

After the selection of k, the relation between Q_F and g can be determined by analyzing M_F. Fig. 15(c) is a graphic of M_F versus Q_F and g when $f_n = 0.75$. Based on Fig. 15(c), to ensure this constraint from light to full load conditions,

relation between Q_F and g can be approximately obtained with a certain margin:

$$Q_F + 7g < 1.3. \quad (29)$$

Constraint 3-2-4: $M_F(f_n = 1.25) < 0.225$.

Fig. 15(d) is a graphic of M_F versus Q_F and g when $f_n = 1.25$. By approximating the intersection curve of the voltage gain and $M_F = 0.225$ plane, Q_F and g need to satisfy the following relation to ensure $M_F < 0.225$:

$$\frac{Q_F^2}{0.95^2} + \frac{(g - 0.4)^2}{0.31^2} > 1. \quad (30)$$

On one hand, by combining (21) and (27), it can be concluded that g needs to be greater than 0.0925. On the other hand, it can be seen that if (30) can be satisfied under light load condition (i.e., small Q_F), it is satisfied under any load conditions. Hence, $g < 0.1$ is a reasonable choice. Therefore, the final range of g can be set as:

$$0.0925 < g < 0.1. \quad (31)$$

B. RESONANT TANK CURRENTS POINT OF VIEW

Based on the preliminary selection in Section IV-A, this section will finalize the parameters from the perspective of reducing the resonant tank currents. To avoid complex formula calculations and provide reliable results, a MATLAB-aid parameter selection method is adopted. Within the set selection ranges and selection steps, the parameter results that can meet the constraints in Section IV-A while having the minimum resonant tank currents will be filtered automatically. Since k and n have been determined, it is only necessary to determine the values of L_m, L_a, and C_r in this section. Two constraints for L_m, L_a, and C_r selection ranges can be summarized as follows:

Constraint 1: To achieve ZVS, turn-off currents of the inverter switch in forward and backward modes should both be greater than zero, which ensure the complete charging and discharging to the parasitic capacitors. Meanwhile, too large turn-off currents should also be avoided, otherwise they will bring excessive turn-off losses. Thus, based on the rated power of 500W and rated voltage levels, the approximate ranges of L_m and L_a can be determined.

Constraint 2: The main resonant frequency f_{r1} of the converter is set to around 100kHz, and the approximate range of C_r can thus be obtained by (2) and constraint 1.

With these two constraints, the final parameter selection ranges and steps are determined as Table 6 shown.

TABLE 6. Ranges and steps for parameters optimization.

Optimization parameters	Selection ranges		Selection steps
	Minimum	Maximum	
Inductance L_m	60μH	900μH	15μH
Inductance L_a	$(60/n^2)$μH	$(900/n^2)$μH	$(15/n^2)$μH
Capacitance C_r	90nF	1800nF	45nF

When the main resonant frequency f_{r1} is within 98-102 kHz, the final selection results that can meet the constraints in Section IV-A while having the lowest IRMSCs, ORMSCs, inverter switch turn-off currents, and resonant inductors RMS currents can be obtained by MATLAB. For ease of operation in practical, by approximating the MATLAB selection results, the final parameter values are shown in Table 7.

TABLE 7. Experimental parameters.

Parameters	Values and/or types
Rated power P_n	500W
Rated value of U_H	200V
Range/rated value of U_L	45V-55V/50V
Main resonant frequency f_{r1}	100kHz
Maximum range of f_S	75kHz-125kHz
Inductor L_r	45μH (PQ2625-PC95)
Magnetizing inductor L_m	135μH (PQ3535-PC95)
Transformer turns-ratio n	3
Inductor L_a	13μH (PQ2620-PC95)
Capacitor C_r	680nF (WIMA/film)
HVS MOSFETs: $S_1 \sim S_4$	IXFH50N30Q3
LVS MOSFETs: $Q_1 \sim Q_4$	IPB036N12N3G

V. EXPERIMENTS

To verify the theoretical analyses of LLCL, a 500-W prototype presented in Fig. 16 is established and evaluated. The experimental parameters are listed in Table 7.
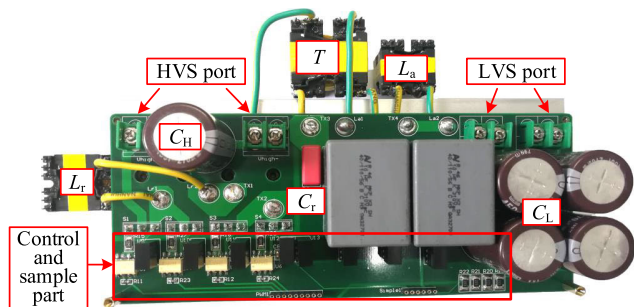

FIGURE 16. Photograph of the LLCL prototype built in the laboratory.

Fig. 17 shows the experimental waveforms in forward mode. Each subfigure shows the driving voltage of S_1, u_{S1_G}, drain-source voltage of S_1, u_{S1}, drain-source voltage of Q_1, u_{Q1}, and the current through L_r, i_{Lr_F}. The waveforms shown in Fig. 17(a), (b), and (c) are all tested at $U_H = 200V$ and $R_{o\_L} = 5\Omega$, whereas f_S are 83kHz, 100kHz, and 115kHz, respectively. By observing u_{Q1}, it can be seen that U_L equals 55V at 83kHz, 50V at 100kHz, and 45V at 115kHz, which means the demand voltage regulation range can be achieved within f_S range of 83-115kHz. From the waveforms of i_{Lr_F}, it can be found that DCM occurs when $f_S = 83$kHz and CCM occurs when $f_S = 100$kHz and 115kHz. By observing Fig. 17(b), the complete sinusoidal waveform of i_{Lr_F} also means 100kHz is the main resonant frequency. Fig. 17(d) is tested at $U_H = 200V$, $f_S = 100$kHz, and $R_{o\_L} = 25\Omega$
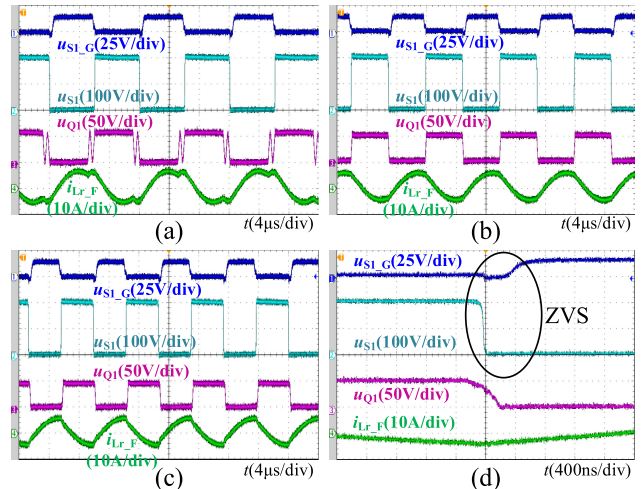

FIGURE 17. Experimental waveforms in forward mode. (a) 83kHz, $R_{o\_L} = 5\Omega$, (b) 100kHz, $R_{o\_L} = 5\Omega$, (c) 115kHz, $R_{o\_L} = 5\Omega$, (d) 100kHz, $R_{o\_L} = 25\Omega$.

(20% of full load, 100W). By observing u_{S1_G} and u_{S1}, it can be seen that ZVS can still be realized even under a very light load condition.

Meanwhile, the experimental waveforms in backward mode are shown in Fig. 18. Each subfigure shows the driving voltage of Q_1, u_{Q1_G}, drain-source voltage of Q_1, u_{Q1}, drain-source voltage of S_1, u_{S1}, and the current through C_r, i_{Cr_B}. The waveforms shown in Fig. 18(a), (b), and (c) are all tested at $R_{o\_H} = 80\Omega$, whereas U_L are 45V, 50V, and 55V, respectively. When f_S is set to 83kHz in Fig. 18(a), 100kHz in Fig. 18(b), and 115kHz in Fig. 18(c), it can be seen from U_{S1} that different f_S can hold U_H at 200V in all three cases. By observing i_{Cr_B}, it can be noticed that the converter is in DCM in Fig. 18(a), and is in CCM in Fig. 18(b) and (c). Also, the main resonant frequency of 100kHz can be seen by the
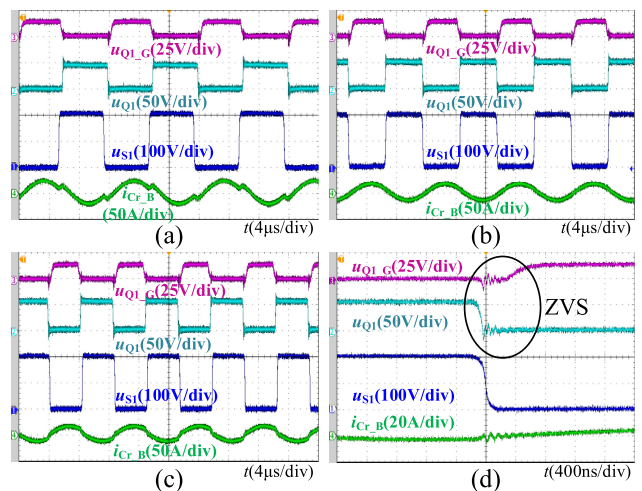

FIGURE 18. Experimental waveforms in backward mode. (a) 83kHz, $R_{o\_H} = 80\Omega$, (b) 100kHz, $R_{o\_H} = 80\Omega$, (c) 115kHz, $R_{o\_H} = 80\Omega$, (d) 125kHz, $R_{o\_H} = 400\Omega$.
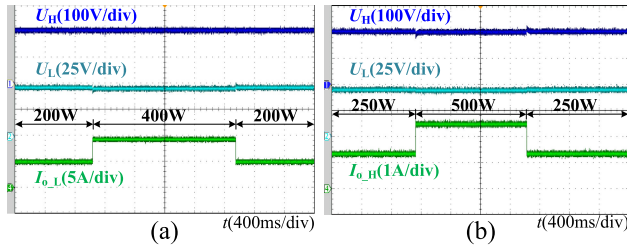
FIGURE 19. Dynamic process waveforms. (a) Forward mode with output power step changed from 200W to 400W to 200W, U_L = 45V, (b) Backward mode with output power step changed from 250W to 500W to 250W, U_L = 45V.
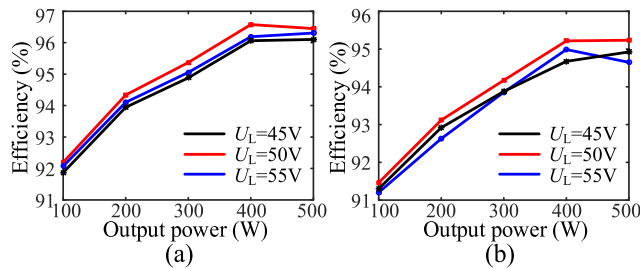

FIGURE 20. Efficiency curves of LLCL converter. (a) Forward mode, (b) Backward mode.

sinusoidal waveform i_{Cr_B} in Fig. 18(b). Fig. 18(d) is tested at U_H = 200V, f_S = 125kHz, and R_{o_H} = 400Ω (20% of full load, 100W). u_{Q1_G} and u_{Q1} indicate that LLCL can also achieve ZVS in backward mode over a wide load range.

Fig. 19(a) shows the dynamic process in forward mode, when the output power is step changed between 200W and 400W (reflected in the change of the dc output current I_{o_L}). It can be noticed that with a constant U_H of 200V, U_L can be maintained at 45V by the output voltage closed loop control. Moreover, Fig. 19(b) shows the dynamic process in backward mode, when the output power is step changed between 250W and 500W (reflected in the change of the dc output current I_{o_H}). With a constant U_L of 45V, U_H can be also maintained at 200V. The stability of LLCL can be confirmed by these waveforms.

Finally, the measured efficiency curves of the prototype based on the same U_H (200V), different output power, and different U_L are demonstrated in Fig. 20. Fig. 20(a) and (b) show the efficiency results in forward and backward mode, respectively. The highest efficiency point (96.58%) occurs in forward mode with U_L = 50V and 400W output power. Even with a very light output power (100W), since ZVS can still be achieved, the converter also has the efficiency greater than 91% in both power flow modes.

VI. CONCLUSIONS

This paper proposes a bidirectional LLCL resonant dc-dc converter. By employing a parallel-connected inductors structure into conventional LLC resonant tank, a bidirectional LLC-type structure is thus obtained. As a result, the proposed LLCL converter harvests the excellent gain

and soft-switching features in bidirectional power flow applications. In addition, the analysis of the LLCL resonant tank fully demonstrates that the parallel-connected inductors structure in LLCL can effectively reduce the resonant tank currents and the resonant capacitor voltage stress when compared with Bi-LLC and CLLC under the same working conditions. Stated thus, LLCL will have great potential to reduce the power losses, reduce the resonant capacitor cost and promote the reliability. Based on battery applications in ESSs, a parameter design method considering the voltage gain range and the reduction of resonant tank currents is conducted. In the end, the experimental results based on a 500-W prototype are displayed to verify the theoretical analyses. The maximum efficiency is 96.58%. In the future, magnetic integration techniques for LLCL will be further studied, which will play a positive role in the magnetic losses reduction and power density improvement.

APPENDIX

For Bi-LLC converter shown in Fig. 2(a), when $n = 1$, time domain expressions of the resonant tank input current ($i_{in\_F}(t)$ in forward mode, $i_{in\_B}(t)$ in backward mode) and output current ($i_{out\_F}(t)$ in forward mode, $i_{out\_B}(t)$ in backward mode) are:

$$
\begin{cases}
i_{in\_F}(t) = \dfrac{4U_L}{\pi R_{eq\_L}} \sin \omega_r t - \dfrac{k\pi U_L}{2gQ_F R_{eq\_L}} \cos \omega_r t \\
\quad + \dfrac{kU_L}{Q_F R_{eq\_L}} \omega_r t - \dfrac{k\pi U_L}{2Q_F R_{eq\_L}} \\
i_{in\_B}(t) = \dfrac{4U_H}{\pi R_{eq\_H}} \sin \omega_r t - \dfrac{k\pi U_H}{2Q_B R_{eq\_H}} \cos \omega_r t \\
\quad + \dfrac{kU_H}{gQ_B R_{eq\_H}} \omega_r t - \dfrac{k\pi U_H}{2gQ_B R_{eq\_H}} \\
i_{out\_F}(t) = \dfrac{4U_L}{\pi R_{eq\_L}} \sin \omega_r t - \dfrac{k\pi U_L}{2gQ_F R_{eq\_L}} \cos \omega_r t \\
\quad - \dfrac{kU_L}{gQ_F R_{eq\_L}} \omega_r t + \dfrac{k\pi U_L}{2gQ_F R_{eq\_L}} \\
i_{out\_B}(t) = \dfrac{4U_H}{\pi R_{eq\_H}} \sin \omega_r t - \dfrac{k\pi U_H}{2Q_B R_{eq\_H}} \cos \omega_r t \\
\quad - \dfrac{kU_H}{Q_B R_{eq\_H}} \omega_r t + \dfrac{k\pi U_H}{2Q_B R_{eq\_H}}.
\end{cases} \tag{A.1}
$$

By means of (A.1), when t is equal to the half switching period $T_S/2$, turn-off current of the inverter switch (i_{off_F} in forward mode, i_{off_B} in backward mode) of Bi-LLC can be calculated as:

$$
\begin{cases}
i_{off\_F} = i_{in\_F}(\dfrac{T_S}{2}) = \dfrac{k\pi U_L(g+1)}{2gQ_F R_{eq\_L}} \\
i_{off\_B} = i_{in\_B}(\dfrac{T_S}{2}) = \dfrac{k\pi U_H(g+1)}{2gQ_B R_{eq\_H}}.
\end{cases} \tag{A.2}
$$

Also, the currents through L_a ($i_{La\_F}(t)$ in forward mode, $i_{La\_B}(t)$ in backward mode), L_m ($i_{Lm\_F}(t)$ in forward mode, $i_{Lm\_B}(t)$ in backward mode), and L_r ($i_{Lr\_F}(t)$ in forward mode, $i_{Lr\_B}(t)$ in backward mode) of Bi-LLC can be shown

as:

$$
\begin{cases}
i_{\text{La\_F}}(t) = \dfrac{kU_{\text{L}}}{gQ_{\text{F}}R_{\text{eq\_L}}}\omega_{\text{r}}t - \dfrac{k\pi U_{\text{L}}}{2gQ_{\text{F}}R_{\text{eq\_L}}} \\[2ex]
i_{\text{La\_B}}(t) = \dfrac{kU_{\text{H}}}{gQ_{\text{B}}R_{\text{eq\_H}}}\omega_{\text{r}}t - \dfrac{k\pi U_{\text{H}}}{2gQ_{\text{B}}R_{\text{eq\_H}}} \\[2ex]
i_{\text{Lm\_F}}(t) = \dfrac{kU_{\text{L}}}{Q_{\text{F}}R_{\text{eq\_L}}}\omega_{\text{r}}t - \dfrac{k\pi U_{\text{L}}}{2Q_{\text{F}}R_{\text{eq\_L}}} \\[2ex]
i_{\text{Lm\_B}}(t) = \dfrac{kU_{\text{H}}}{Q_{\text{B}}R_{\text{eq\_H}}}\omega_{\text{r}}t - \dfrac{k\pi U_{\text{H}}}{2Q_{\text{B}}R_{\text{eq\_H}}} \\[2ex]
i_{\text{Lr\_F}}(t) = \dfrac{4U_{\text{L}}}{\pi R_{\text{eq\_L}}}\sin\omega_{\text{r}}t - \dfrac{k\pi U_{\text{L}}}{2gQ_{\text{F}}R_{\text{eq\_L}}}\cos\omega_{\text{r}}t \\[2ex]
i_{\text{Lr\_B}}(t) = \dfrac{4U_{\text{H}}}{\pi R_{\text{eq\_H}}}\sin\omega_{\text{r}}t - \dfrac{k\pi U_{\text{H}}}{2Q_{\text{B}}R_{\text{eq\_H}}}\cos\omega_{\text{r}}t.
\end{cases} \tag{A.3}
$$

Moreover, the resonant capacitor voltage expressions of Bi-LLC ($u_{\text{Cr\_F}}(t)$ in forward mode, $u_{\text{Cr\_B}}(t)$ in backward mode) can be given as:

$$
\begin{cases}
u_{\text{Cr\_F}}(t) = \dfrac{-k\pi U_{\text{L}}}{2g}\left(\dfrac{8gQ_{\text{F}}}{k\pi^2}\cos\omega_{\text{r}}t + \sin\omega_{\text{r}}t\right) \\[2ex]
u_{\text{Cr\_B}}(t) = \dfrac{-k\pi U_{\text{H}}}{2}\left(\dfrac{8Q_{\text{B}}}{k\pi^2}\cos\omega_{\text{r}}t + \sin\omega_{\text{r}}t\right).
\end{cases} \tag{A.4}
$$

REFERENCES

[1] K.-Y. Lo, Y.-M. Chen, and Y.-R. Chang, "Bidirectional single-stage grid-connected inverter for a battery energy storage system," *IEEE Trans. Ind. Electron.*, vol. 64, no. 6, pp. 4581–4590, Jun. 2017.

[2] V. Karthikeyan and R. Gupta, "Distributed power flow control using cascaded multilevel isolated bidirectional DC-DC converter with multi-phase shift modulation," *IET Power Electron.*, vol. 12, no. 11, pp. 2996–3003, Sep. 2019.

[3] J.-C. Wu, H.-L. Jou, and I.-H. Chiu, "Interleaved multi-level power converter for a battery energy storage system," *IET Power Electron.*, vol. 12, no. 3, pp. 498–504, Mar. 2019.

[4] Y.-E. Wu and I.-C. Chen, "Novel integrated three-port bidirectional DC/DC converter for energy storage system," *IEEE Access*, vol. 7, pp. 104601–104612, 2019.

[5] N. Elsayad, H. Moradisizkoohi, and O. A. Mohammed, "Design and implementation of a new transformerless bidirectional DC-DC converter with wide conversion ratios," *IEEE Trans. Ind. Electron.*, vol. 66, no. 9, pp. 7067–7077, Sep. 2019.

[6] F. Xue, R. Yu, and A. Q. Huang, "A 98.3% efficient GaN isolated bidirectional DC-DC converter for DC microgrid energy storage system applications," *IEEE Trans. Ind. Electron.*, vol. 64, no. 11, pp. 9094–9103, Nov. 2017.

[7] O. Demirel, U. Arifoglu, and K. Kalayci, "Novel three-level T-type isolated bidirectional DC-DC converter," *IET Power Electron.*, vol. 12, no. 1, pp. 61–71, Jan. 2019.

[8] S. Shao, H. Chen, X. Wu, J. Zhang, and K. Sheng, "Circulating current and ZVS-on of a dual active bridge DC-DC converter: A review," *IEEE Access*, vol. 7, pp. 50561–50572, 2019.

[9] M. N. Kheraluwala, R. W. Gascoigne, D. M. Divan, and E. D. Baumann, "Performance characterization of a high-power dual active bridge DC-to-DC converter," *IEEE Trans. Ind. Appl.*, vol. 28, no. 6, pp. 1294–1301, Nov. 1992.

[10] B. Zhao, Q. Song, W. Liu, and Y. Sun, "Overview of dual-active-bridge isolated bidirectional DC-DC converter for high-frequency-link power-conversion system," *IEEE Trans. Power Electron.*, vol. 29, no. 8, pp. 4091–4106, Aug. 2014.

[11] S. Shao, M. Jiang, W. Ye, Y. Li, J. Zhang, and K. Sheng, "Optimal phase-shift control to minimize reactive power for a dual active bridge DC-DC converter," *IEEE Trans. Power Electron.*, vol. 34, no. 10, pp. 10193–10205, Oct. 2019.

[12] Z. Guo, D. Sha, and K. Song, "Output-series connected dual active bridge converters for zero-voltage switching throughout full load range by employing auxiliary LC networks," *IEEE Trans. Power Electron.*, vol. 34, no. 6, pp. 5549–5562, Jun. 2019.

[13] Z. Guo and D. Sha, "Dual-active-bridge converter with parallel-connected full bridges in low-voltage side for ZVS by using auxiliary coupling inductor," *IEEE Trans. Ind. Electron.*, vol. 66, no. 9, pp. 6856–6866, Sep. 2019.

[14] R. P. Twiname, D. J. Thrimawithana, U. K. Madawala, and C. A. Baguley, "A new resonant bidirectional DC-DC converter topology," *IEEE Trans. Power Electron.*, vol. 29, no. 9, pp. 4733–4740, Sep. 2014.

[15] R. P. Twiname, D. J. Thrimawithana, U. K. Madawala, and C. A. Baguley, "A dual-active bridge topology with a tuned CLC network," *IEEE Trans. Power Electron.*, vol. 30, no. 12, pp. 6543–6550, Dec. 2015.

[16] S. Hu, X. Li, and A. K. S. Bhat, "Operation of a bidirectional series-resonant converter with minimized tank current and wide ZVS range," *IEEE Trans. Power Electron.*, vol. 34, no. 1, pp. 904–915, Jan. 2019.

[17] M. Yaqoob, K. H. Loo, and Y. M. Lai, "A four-degrees-of-freedom modulation strategy for dual-active-bridge series-resonant converter designed for total loss minimization," *IEEE Trans. Power Electron.*, vol. 34, no. 2, pp. 1065–1081, Feb. 2019.

[18] H.-D. Gui, Z. Zhang, X.-F. He, and Y.-F. Liu, "A high voltage-gain LLC micro-converter with high efficiency in wide input range for PV applications," in *Proc. IEEE Appl. Power Electron. Conf. Expo. (APEC)*, Fort Worth, TX, USA, Mar. 2014, pp. 637–642.

[19] D. Huang, F. C. Lee, and D. Fu, "Classification and selection methodology for multi-element resonant converters," in *Proc. 26th Annu. IEEE Appl. Power Electron. Conf. Expo. (APEC)*, Fort Worth, TX, USA, Mar. 2011, pp. 558–565.

[20] D. Huang, D. Fu, F. C. Lee, and P. Kong, "High-frequency high-efficiency CLL resonant converters with synchronous rectifiers," *IEEE Trans. Ind. Electron.*, vol. 58, no. 8, pp. 3461–3470, Aug. 2011.

[21] T. Jiang, J. Zhang, X. Wu, K. Sheng, and Y. Wang, "A bidirectional LLC resonant converter with automatic forward and backward mode transition," *IEEE Trans. Power Electron.*, vol. 30, no. 2, pp. 757–770, Feb. 2015.

[22] H. Wu, S. Ding, K. Sun, L. Zhang, Y. Li, and Y. Xing, "Bidirectional soft-switching series-resonant converter with simple PWM control and load-independent voltage-gain characteristics for energy storage system in DC microgrids," *IEEE J. Emerg. Sel. Topics Power Electron.*, vol. 5, no. 3, pp. 995–1007, Sep. 2017.

[23] H. Wu, K. Sun, Y. Li, and Y. Xing, "Fixed-frequency PWM-controlled bidirectional current-fed soft-switching series-resonant converter for energy storage applications," *IEEE Trans. Ind. Electron.*, vol. 64, no. 8, pp. 6190–6201, Aug. 2017.

[24] X. Tang, H. Wu, W. Hua, Z. Yu, and Y. Xing, "Three-port bidirectional series-resonant converter with first-harmonic-synchronized PWM," *IEEE J. Emerg. Sel. Topics Power Electron.*, early access, Feb. 20, 2020, doi: 10.1109/JESTPE.2020.2975164.

[25] J.-H. Jung, H.-S. Kim, M.-H. Ryu, and J.-W. Baek, "Design methodology of bidirectional CLLC resonant converter for high-frequency isolation of DC distribution systems," *IEEE Trans. Power Electron.*, vol. 28, no. 4, pp. 1741–1755, Apr. 2013.

[26] P. He and A. Khaligh, "Comprehensive analyses and comparison of 1 kW isolated DC-DC converters for bidirectional EV charging systems," *IEEE Trans. Transport. Electrific.*, vol. 3, no. 1, pp. 147–156, Mar. 2017.

[27] B. Li, Q. Li, F. C. Lee, Z. Liu, and Y. Yang, "A high-efficiency high-density wide-bandgap device-based bidirectional on-board charger," *IEEE J. Emerg. Sel. Topics Power Electron.*, vol. 6, no. 3, pp. 1627–1636, Sep. 2018.

[28] X. Lu and H. Wang, "A highly efficient multifunctional power electronic interface for PEV hybrid energy management systems," *IEEE Access*, vol. 7, pp. 8964–8974, 2019.

[29] C. Zhang, P. Li, Z. Kan, X. Chai, and X. Guo, "Integrated half-bridge CLLC bidirectional converter for energy storage systems," *IEEE Trans. Ind. Electron.*, vol. 65, no. 5, pp. 3879–3889, May 2018.

[30] J.-Y. Lee, Y.-S. Jeong, and B.-M. Han, "An isolated DC/DC converter using high-frequency unregulated LLC resonant converter for fuel cell applications," *IEEE Trans. Ind. Electron.*, vol. 58, no. 7, pp. 2926–2934, Jul. 2011.

[31] Y. Chen, H. Wang, Z. Hu, Y.-F. Liu, X. Liu, J. Afsharian, and Z. Yang, "LCLC converter with optimal capacitor utilization for hold-up mode operation," *IEEE Trans. Power Electron.*, vol. 34, no. 3, pp. 2385–2396, Mar. 2019.

XIAOCHEN MA was born in Hebei, China, in 1995. He received the B.S. degree in electrical engineering from Fuzhou University, Fuzhou, Fujian, China, in 2018. He is currently pursuing the M.S. degree in electrical engineering with Tianjin University, Tianjin, China.

His current research interest includes dc-dc resonant converters.

HUAKUN BI (Member, IEEE) was born in Shandong, China. He received the B.S. degree in electrical engineering from the Changchun University of Technology, Changchun, Jilin, China, in 2013, the M.S. degree in electrical engineering from the Hebei University of Technology, Tianjin, China, in 2016, and the Ph.D. degree in electrical engineering from Tianjin University, Tianjin, in 2020.

His current research interests include dc-dc converters, electric vehicle, and dc microgrids.

PING WANG (Member, IEEE) was born in Tianjin, China, in 1959. She received the B.S., M.S., and Ph.D. degrees in electrical engineering from Tianjin University, Tianjin, in 1981, 1991, and 2005, respectively.

She joined Tianjin University, as a Teacher and a Researcher, in 1981, where she is currently working as a Professor. Her current research interests include power electronic control of renewable energy sources, PWM converters, and intelligent detection and control.

ZHISHUANG WANG was born in Shanxi, China, in 1994. She received the B.S. degree in electrical engineering from China Three Gorges University, Yichang, Hubei, China, in 2016. She is currently pursuing the Ph.D. degree in electrical engineering with Tianjin University, Tianjin, China.

Her current research interests include dc-dc converters and dc microgrids.

• • •